Computers in Biology and Medicine 110 (2019) 265–275

Contents lists available at ScienceDirect

Computers in Biology and Medicine

journal homepage: www.elsevier.com/locate/compbiomed

Mathematical synthesis of the cortical circulation for the whole mouse brain-part I. theory and image integration

Andreas Linninger[a,b,*], Grant Hartung[a], Shoale Badr[a], Ryan Morley[a]

[a] Department of Bioengineering, University of Illinois at Chicago, Chicago, IL, USA
[b] Department of Neurosurgery, University of Illinois at Chicago, Chicago, IL, USA

ARTICLE INFO

Keywords:
Cerebral circulation
Vascular synthesis
Microcirculation
Biphasic blood flow
Mouse brain

ABSTRACT

Microcirculation plays a significant role in cerebral metabolism and blood flow control, yet explaining and predicting functional mechanisms remains elusive because it is difficult to make physiologically accurate mathematical models of the vascular network. As a precursor to the human brain, this paper presents a computational framework for synthesizing anatomically accurate network models for the cortical blood supply in mouse. It addresses two critical deficiencies in cerebrovascular modeling. At the microscopic length scale of individual capillaries, we present a novel synthesis method for building anatomically consistent capillary networks with loops and anastomoses (=microcirculatory closure). This overcomes shortcomings in existing algorithms which are unable to create closed circulatory networks. A second critical innovation allows the incorporation of detailed anatomical features from image data into vascular growth. Specifically, computed tomography and two photon laser scanning microscopy data are input into the novel synthesis algorithm to build the cortical circulation for the entire mouse brain *in silico*. Computer predictions of blood flow and oxygen exchange executed on synthetic large-scale network models are expected to elucidate poorly understood functional mechanisms of the cerebral circulation.

1. Introduction

Detailed anatomical models of cerebral circulation can serve as virtual surrogates enabling quantitative analysis of functional mechanisms in the brain. To ensure consistency, digital vascular models should match physiological and anatomical topology of in vivo cerebral angioarchitecture. Image-segmentation is an essential technique to acquire necessary physiological information such as number, position, and connectivity of arterial and venous segments. Accordingly, several groups have created microcirculatory models from neuroimages [1–5]. However, segmentation of image data faces several challenges. The number of microvascular segments is staggering; the human brain is estimated to have more than 10 billion capillaries, or ~8,000 segments/mm^3 [5]. Morphometric studies on cadaver brains [5,6] are also problematic, because blood flow ceases and capillary networks may collapse post-mortem. In vivo imaging acquisition looks at microcirculation through a cranial windows that affords only a narrow glimpse of the brain covering a range of hundreds of microns to a millimeter. At the edges of the imaging window, it is unavoidable that all pial connections of larger arteries, deeper arterioles, and capillaries are severed. These artificial cut-off boundaries expose mathematical models to boundary effects, whose detrimental impact on reliable predictions has been pointed out by Lorthois [3,7]. Moreover, raw neuroimaging data require extensive post-processing to fill gaps, remove dangling segments, or reconcile noisy or missing information at the imaging threshold [8]. No single imaging modality can directly image all blood vessels in the brain at the macro- and micro-anatomical scale reliably, although there is progress towards this goal [9–11]. This limitation leaves gaps in data acquired at the macro [12–15] and micro [1,4,5] anatomical scale.

Synthetic vascular models offer an alternative to purely image-based approaches that may suffer from uncertainty in the microscale [16–19]. Bui et al. used a fractal tree model with a level set distance function [20]. Schreiner and Karch [21–26] generated coronary arterial trees artificially by combining the principle of volume minimization (=minimum blood lumen) with random segment addition. Their *constrained constructive optimization* (CCO) algorithm is capable of synthesizing branched structures that resemble natural arterial trees. They successfully created physiologically sound arterial trees in flat sheets (2D) and slabs (3D). The algorithm also synthesized trees whose morphometrics closely matched coronary arteries. However, constructive synthesis of tree-like structures breaks down for microcirculatory

* Corresponding author. Department of Bioengineering, University of Illinois at Chicago, Chicago, IL, USA.
E-mail address: linninge@uic.edu (A. Linninger).

https://doi.org/10.1016/j.compbiomed.2019.05.004
Received 21 February 2019; Received in revised form 25 April 2019; Accepted 4 May 2019

networks, because they have loops and anastomoses, thus they are not binary trees. It is not possible to perform tree lumen minimization by recursion, thus rendering the required combinatorial optimization intractable. Accordingly, the most critical limitation of classical CCO is its inability to create circulatory networks which connect the arterial side to the venous circulation through a physiologically consistent capillary bed.

Recently, Linninger presented an alternative method for building realistic microcirculatory beds using Voronoi tessellation [27]. They synthesized the cortical blood supply in a sizable section of the human cortex with physiologically sound multi-scale representation of arteries, the capillary bed and the venous circulation [27]. However, that solution requires expensive Delaunay and Voronoi tessellations followed by diameter smoothing procedures. This article introduces a novel microvascular closure that employs construction principles directly, so that closed networks encompassing an arterial and a venous tree with capillary connection can be synthesized with a single algorithm.

This paper presents a novel methodology entitled image-based Circulatory Network Synthesis (iCNS) that combines the critical advantages of image-based models with synthetic vascular growth. The methodology and implementation sections will present mathematical background and procedures. Section 4 will demonstrate the creation of realistic models for the circulation in major vascular territories (MCA territory) and present the successful application of the methodology to synthesize a realistic model of the cortical circulation for the entire mouse brain.

2. Methodology

Image-based Circulatory Network Synthesis (iCNS) is also based on constrained constructive optimization principles developed by the pioneering work by Karch and Schreiner [21–26]. Foundation of vascular synthesis within a mathematical programming (=optimization) theory has been implied by their work, but not been presented formally. Therefore, we derive constrained constructive optimization principles from a formal mixed integer nonlinear programming (MINLP) framework in Section 2.1. We generalize the method of Karch and Schreiner in two critical aspects: First, a novel scale-invariant nonlinear programming formulation enables the incorporation of anatomical features from image data (Section 2.2). Second, a novel *microcirculatory closure* algorithm for synthesizing capillary networks provides the critically missing connection between arterial and venous circulation (Section 2.3).

2.1. The formal optimization problem

A vascular tree can be created artificially by starting with a single cylindrical segment (=root branch), see Fig. 1. The tree is expanded by spawning additional segments until a desired number of branches is reached. Branches are added by connecting a close segment from an existing branch to a new terminal node at a random location. Branch addition must obey geometrical and physiological constraints to ensure that the artificial tree matches real vascular topology. This is ensured by imposing the objective of minimizing the overall tree volume with the side constraint that blood conveyed through the tree segments perfuse the domain evenly. For each segment addition step, tree volume minimization subject to hemodynamic constraints can be formally expressed as a mixed integer non-linear program (MINLP) given by system (1). It is a global minimization Problem with binary variables, y, that decide the location (=existing branch) where the new segment should be attached. Only one connection can be made at each step as expressed by the logical constraint in (1b). Moreover, morphometric parameters (=segment length and diameters, for nomenclature see Table 1) appear in the highly non-linear resistance computations of fluid flow equations, $F(x, y) = 0$, in eq (1a)

$$\min_{x,y} V(x,y) \tag{1}$$

$$s.t. \quad F(x,y) = 0 \tag{1a}$$

$$\sum_{i=1}^{N} y = 1 \tag{1b}$$

$$x = \{\alpha, p, q\}, \qquad y\epsilon\{0,1\}^N$$

.

Each volume minimization step is a *non-polynomial (NP) hard* problem, because it contains logical (=new possible connection to multiple existing segments) and parametric decisions (=optimal positions Bif(ξ^*, η^*) which in turn determine segment lengths, diameters, resistances, α, blood flows, q, and pressures, p, along the vascular tree). Two *admissible* heuristics help prune the search:

- Only consider N segments closest to the new terminal as possible connections (*near-vicinity heuristic*)
- Search bifurcation locations in the two dimensional subspace spanned by the bifurcation topology (parent node and two child nodes - *planar bifurcation heuristic*).

The near vicinity heuristic allows problem decomposition into independent nonlinear subproblems given in system (2), one *volume minimization* problem, $V(x)$, for each possible connection y, in the N nearest neighborhood of the new terminal node. The first constraint relates flows, q, to pressure drops, p, which is compactly expressed in matrix form using the diagonal resistance matrix, $A = \mathrm{diag}(\alpha(\xi, \eta))$, which holds the segment resistances, $\alpha(\xi, \eta)$, as functions of the unknown bifurcation position, (ξ, η). The incidence matrix C_1 stores the node connectivity for each segment. The second constraint, $C_2\, q = 0$, enforces flow conservation for each node. More details on the use of incidence matrices C_1 and C_2 for formulating network flow problems can be found elsewhere [28–30]. The planar bifurcation heuristic limits the position of new connections to two independent spatial coordinates (ξ, η) inside the bifurcation plane, which reduces the computational burden. The desired solution is the globally best connection (y*) with planar bifurcation coordinates (ξ^*, η^*) that determine associated tree metrics (=length, diameters) which in turn fixes fluid flows and pressures.

For N segments close to new terminal T do (*for each possible connection y do*)

$$\min_{x} V(x)$$

$$s.\,t. \quad \begin{bmatrix} A(\xi,\eta) & -C_1 \\ C_2 & 0 \end{bmatrix} \begin{pmatrix} q \\ p \end{pmatrix} = \begin{pmatrix} 0 \\ 0 \end{pmatrix}$$

$$x = x(\alpha(\xi,\eta)\,,\, p(\xi,\eta),\, q(\xi,\eta)) \tag{2}$$

Problem reduction. Each constrained NLP in eq (2) can be further simplified into a single unconstrained nonlinear function minimization problem in merely two variables (=the bifurcation position, (ξ, η)). The volume in a balanced tree can be precisely determined with the help of eqs (3)–(5) for a desired perfusion ratio $Q_0/\Delta P$ and segment lengths determined by the bifurcation position (ξ, η). *Balancing* the tree brings the substantial benefit that instead of solving for all pressures, p, and flows, q, only the *total tree resistance*, a_0, needs to be computed. Accordingly, the total tree resistance is a function of only the root radius and the total accumulated reduced resistance. In effect, all flows and pressures as well as all branch diameters (except the root diameter, d_0) can be eliminated by recursive formulae. It will be shown that *total tree resistance*, a_0, is only a function of *total diameter-independent resistance* r_0 and the root diameter, d_0.

$$\min_{\xi,\eta} V(d_0(\xi, \eta)) \tag{3}$$

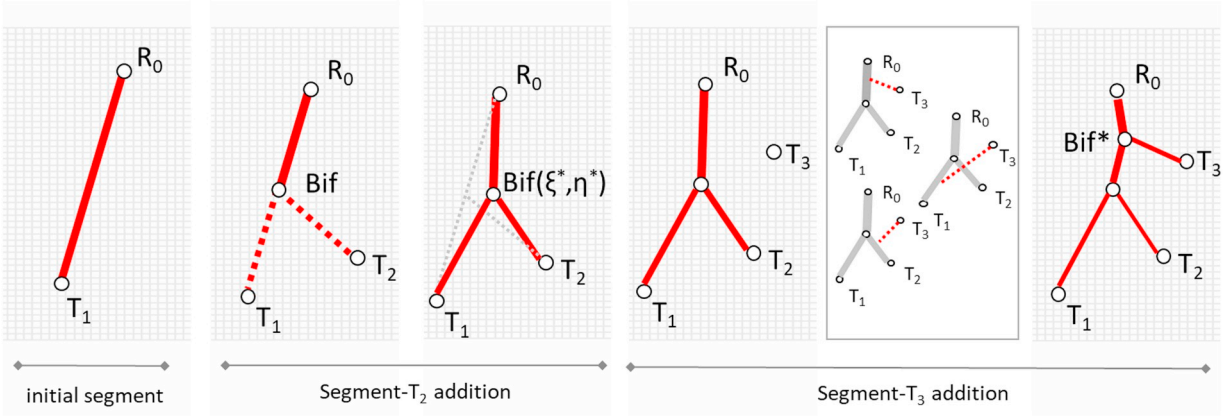

Fig. 1. Overview of CCO method by Schreiner and Karch starting with one segment. Arterial tree growth begins with an initial segment, R_0-T_1. Segment addition at a random point, T_2, defines a new segment, Bif-T_2. The optimal coordinates in the bifurcation plane (ξ^*, η^*) minimize the tree volume and balance the tree by adjusting all segment diameters. Segment-T_3 addition entails a logical decision to select the globally smallest tree out of $N=3$ possible connections, $y=(y_1, y_2, y_3)$ with $y_i \in \{0,1\}$. possible segment connections. In this example, segment addition at the segment root is optimal, $y^*=(1, 0, 0)$. At each stage, the *balanced* tree discharges equal blood flow to all terminal nodes (T_1-T_3).

Table 1
Nomenclature.

Symbol	Description
A	Diagonal resistance matrix
a	Accumulated downstream resistance
Bif (ξ^*, η^*)	Unknown bifurcation position
C_1	Connectivity matrix
C_2	Incidence matrix
d,d_0	Segment diameter, root segment diameter
F(x)	Flow equations (mass, momentum, conservation)
N	Number of possible choices for connecting new terminal
p, p_0, p_t	Vascular nodal pressure, inlet pressure, terminal pressure
Q, Q_0	Vascular flow, root segment flow
r	Accumulated downstream reduced resistance[a]
r_0	root segment reduced resistance = total reduced resistance of tree[a]
V	Vascular tree volume
x	Vector of unknowns (resistances, flows, and pressures)
y	Binary decision vector to choose connection
α	Vascular segment resistance
α_0	root segment resistance
β	Diameter ratio
ξ	x coordinate of bifurcation
κ	Power law parameter (set to 3)
η	y coordinate of bifurcation
ρ	Segment reduced resistance[a]

[a] Reduced resistance is the length-dependent portion of the resistance that does not contain diameter dependence.

$$a_0 Q_0 = \Delta P = P_0 - P_t \quad \Big| \quad a_0 = \frac{r_0}{d_0^4} \tag{4}$$

$$d_0 = \left(r_0 \frac{Q_0}{\Delta P} \right)^{1/4} \tag{5}$$

Recursive total tree resistance computations. Each connected tree segment *i* has resistance, α_i. The *cumulative resistance,* a_i , sums the accumulated resistances of its subtree, as in eq (6), where the subscripts *i*, *j*, and *k* indicate the parent, the existing branch of the tree at a given bifurcation, and the newly added daughter branch, see Fig. 2. Terminal segments with no subtrees have $a_i = \alpha_i$.

$$a_i = \alpha_i + \frac{1}{\frac{1}{a_j} + \frac{1}{a_k}} \tag{6}$$

To obtain the cumulative tree resistance, a_i, it is advantageous to split it into two separate contributions: the diameter-independent *reduced resistance,* r_i, and separated out the segment diameter, d_i. This

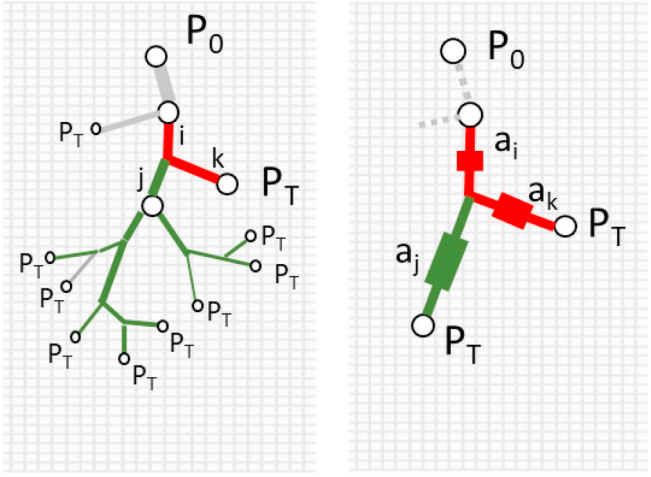

Fig. 2. Recursive tree resistance computations. For a segment addition to the existing segment i, the accumulated subtree resistance (a_j) of the split segment, j, can be recursively computed because all terminal nodes discharge at the terminal pressure P_t. (Nomenclature: parent node, i; existing branch of the tree, j; newly added daughter branch, k).

choice will bring the benefit of enabling the expression of the entire tree resistance in terms of the root diameter d_0. *Reduced resistances* also have a cumulative, r_i, and segment component, ρ_i, as defined in eq (7).

$$a_i = \frac{r_i}{d_i^4} \qquad \alpha_i = \frac{\rho_i}{d_i^4} \tag{7}$$

Fortunately, *cumulative* tree resistances in a balanced tree can be expressed in terms of diameter ratios that only depend on the bifurcation point coordinates, $r_i(\xi, \eta)$. Specifically, a recursive relation for the *reduced resistance*, r_i, can be obtained in terms of diameter ratios β_j, β_k as in eq (8).

$$a_i = \frac{r_i}{d_i^4} = \alpha_i + \frac{1}{\frac{1}{a_j} + \frac{1}{a_k}} = \frac{\rho_i}{d_i^4} + \left(\frac{d_j^4}{r_j} + \frac{d_k^4}{r_k} \right)^{-1}$$

$$r_i = d_i^4 \left(\frac{\rho_i}{d_i^4} + \left(\frac{d_j^4}{r_j} + \frac{d_k^4}{r_k} \right)^{-1} \right) = \rho_i + \left(\frac{d_j^4}{d_i^4}\frac{1}{r_j} + \frac{d_k^4}{d_i^4}\frac{1}{r_k} \right)^{-1} \quad \Big| \quad \beta_j = \frac{d_j}{d_i}, \beta_k = \frac{d_k}{d_i}$$

$$r_i = \rho_i + \left(\frac{\beta_j^4}{r_j} + \frac{\beta_k^4}{r_k} \right)^{-1} \tag{8}$$

Next, we need a method to compute daughter branch ratios. Parent to daughter branch ratios should obey Murray's law expressed in eq (9). We set $\kappa = 3$ following physiological ranges given in the literature [21,31] and is supported by our data analysis in Supplement C, although other choices can be made for other networks.

$$d_i^\kappa = d_k^\kappa + d_j^\kappa \tag{9}$$

Moreover, tree balancing imposes the condition in eq (10) on the diameter ratios of the daughter branch β_j, β_k . The derivation in Supplement A proves that the scalar ratio m is known, because cumulative *diameter-independent* resistances and the number of terminals connected to each daughter branch (N_j and N_k) are set for a segment addition at position (ξ, η).

$$\beta_j = (1 + m^\kappa)^{-1/\kappa}$$

$$\beta_k = (1 + m^{-\kappa})^{-1/\kappa}$$

where

$$m = \left(\frac{\rho_k N_k}{\rho_j N_j} \right)^{1/4} \tag{10}$$

With diameter ratios for all segments now known, the cumulative *diameter-independent* resistance for the entire tree, $r_0(\xi, \eta)$, can be recursively computed. Finally, the tree root diameter, d_0, is found from eq (5) for a desired perfusion flow rate Q_0, and perfusion pressure, ΔP. The total tree volume, V, is computed by adding up cylindrical segment volumes, using eq (10). Actual daughter segment diameters, d_i , can be recursively calculated by multiplying the diameter ratios from the root downwards to segment i as in eq (11), where the index set j signifies the *path* leading from the root segment to segment i.

$$d_i = d_0 \prod_{j=0}^{i} \beta_j \quad j \in \text{path}(i) \tag{11}$$

$$\min_{\xi,\eta} V(d_0(\xi, \eta)) = \sum_{0}^{\text{nSegments}} l_i \, \pi d_i^2 \tag{12}$$

The optimal position (ξ^*, η^*) in the bifurcation plane gives the minimum tree volume for a possible segment connection. The tree with the smallest volume among the N trees with structurally different segment connections gives the *optimal segment addition*. Repeated segment additions, each one performing the global optimization process described in eqs (3–12) yields a synthetic blood flow network with the desired number of segments, *nSegments*.

Illustrated example of the construction principle for generating vascular trees. Constrained constructive segment addition discovered by Karch and Schreiner is illustrated with the help of Fig. 1. *Initiation.* Define a cylindrical segment R_0-T_1 with vascular lumen determined by its length and diameter. Next, randomly choose end point coordinates for a new branch, (terminal node T_2). Tentatively connect T_2 to the middle of the initial segment at location Bif. The simple vascular tree has now three segments (R_0-Bif, Bif-T_1, and Bif-T_2). All diameters are precisely computed to *balance* the tree, a physiological condition that will ensure uniform tissue perfusion by discharging exactly the same blood flow in the terminal nodes (T_1 and T_2). Moreover, Murray's law sets parent to daughter diameter ratios [32]. Next, move the bifurcation coordinates, Bif (ξ, η), to minimize the tree volume, while maintaining the tree *balanced* by segment radii adjustments. The optimal position, Bif (ξ^*, η^*) , gives the desired minimal volume tree.

Continuation. Next, begin another segment conveying blood to a new random terminal location, T_2. From T_2, three structurally different connections, each one to another existing tree segment, are possible. From among the three optimized candidate trees, the global minimum is chosen, here $y^* = (1, 0, 0)$. Repeated segment addition gradually builds large *balanced* vascular trees with minimum volume.

2.2. Image-guided segment addition

The original CCO is well suited for synthesizing space-filling trees, but specific anatomical configurations for organs with complex anatomy are not amenable to constructive growth. For example, the special arrangement of arteries in the Circle of Willis need not be *synthesized*. Instead, it is more practical to incorporate specific anatomical configurations directly from neuroimage or anatomical atlas data. Our new construction methodology has two options to integrate anatomical information:

- Growth from backbone
- Physiological constraints from neuroimages (sample-guided segment addition)

Growth from backbone. This paradigm enables the initiation of vascular synthesis from an existing binary tree (*backbone*) with known connectivity and dimensions (point coordinates, segment length and diameters obtained from an image). Fine-grained additional segments can be added by tree minimization with backbone geometry remaining fixed. If desired, original diameter measurements obtained from image segmentation software [33,34] can be imposed on the backbone segments after the growth algorithm has completed.

Physiological constraints from neuroimages (sample-guided segment addition). We propose to enforce physiological constraints by *SampleGenerator* operators that precisely control subspaces where anatomical segment growth should occur. Using well-established computational meshing methods, arbitrarily complex shapes can be precisely delineated.

2.3. Synthesis of closed networks (=microvascular closure)

Constructive synthesis of tree-like structures breaks down for microcirculatory networks, because loops and anastomoses break the binary tree logic. The required tree lumen minimization cannot be performed recursively, so that segment addition becomes an intractable combinatorial optimization problem. Thus, CCO by Karch and Schreiner is not able to create circulatory networks, which connect the arterial side to the venous circulation.

To overcome the limitation of CCO, we introduce a novel microvascular closure. We create *circulatory networks* whose arterial side connects to the venous circulation through a physiologically consistent capillary bed. A *TerminalNodeSampleGenerator* directs segment formation between each open arterial terminal (=nodes at the precapillary and capillary level) to a nearby venous segment (=near terminal venous segments). The pseudocode listed in Supplement D naturally "grows" contiguous connections between the arterial and venous trees. The microcirculatory closure produces circulatory models with arterial and venous trees linked by a network-like capillary water shed region. When all arterial terminals are attached to the venous segments (=connected), the process is repeated for open venous terminals.

2.4. Neuroimage data for validation of synthetic growth

We based main anatomical features of the large arteries and veins on data acquired with μCT [28,35] and mouse atlases [36]. Microvascular network growth was validated with metrics from two-photon laser scanning microscopy (2PLSM) data acquired previously [4]. More details on data acquisition are given in Supplement F.

2.5. Implementation

This section provides guidelines for implementing the proposed algorithmic framework on existing computer hardware. An overview of the information flow diagram and pseudocodes are given in Supplement B.

Binary tree representation. Vascular trees can be conveniently encoded as binary graphs. An object-oriented implementation should include two key attributes: An *adjacency matrix (*faceMx, C_1*)* whose row indices correspond to vascular segment indices, and row entries holding segment point indices (=two element integer array of point indices). The *point coordinate matrix (*ptCoordMx*)* is a double precision matrix where each row encodes the point coordinates of the corresponding point (=three element array of double precision). The constructor allocates contiguous memory blocks for a desired number of segment additions, with *Npoints* and *Nsegments* serving as counters for the number of nodes and vascular segments, respectively. The binary graph class also has iterators to navigate to binary tree structures recursively: traverse tree upwards from terminal node, traverse tree downwards from root node.

Sample generators. Sample generators are *functors* that control terminal nodal positions during segment addition. A base class implementation of a *TriangleSampleGenerator* is given in Supplement E. *GeometricGenerators* produce random coordinates confined to 2D surfaces or three-dimensional volumes (analytical functions, Rectangle, Circle, Slab, Cube, Cylinder sampler). *MeshSampleGenerator* issues sample points from anatomical surfaces (STL files), or within the cortical volume (3D Carthesian, tetrahedral unstructured or hexahedral structured meshes [37]). Computational meshes can be reconstructed from neuroimage data [33,34]. *SampleGenerators* can also hold a hard coded (predefined), editable list of sample coordinates. For example, the *TerminalNodeSampleGenerator* supplies coordinates of terminals of arterial and venous sections of an emerging (=still unconnected) vascular network. Pseudocodes for a selection of sample generators are listed in Supplement E.

Strategy factory class. The vascular strategy follows the *factory* design pattern. It owns all the data structures (binary arterial and venous trees) and provides the application with control over different stages of growth (sample generators and constraint *functors* [38]). It also keeps counters for the current and desired number of segments additions.

Anatomical constraints in arterial and venous generation. Arterial trees can be synthesized from a backbone, unsupervised growth on an anatomical surface (cortical surface), or a tissue space (subcortical gray matter) based on 3D image data. In each case, *SampleGenerators* can be customized to the needs of the respective anatomy. Venous trees can be created with the same methods as arterial trees when observing lower perfusion pressures (ΔP_A = 40–60 mmHg, ΔP_V = 10–30 mmHg) which produces thicker (=lower resistance) branches for the same perfusion rate, Q_0. Since arterial and venous trees inhabit the same tissue space, collisions between the main branches or individual sections should be avoided.

In case a new sample is too close to a prior terminal, it can be discarded and replaced with a new random point. Specifically, terminal node duplication between the arterial and venous sides is prevented by a vicinity test (*is-close procedure)*. Significant performance enhancements can be achieved when supplying properly spaced sample sets a-priori (*SampleGeneratorFromPointList*), instead of performing vicinity search during each step of the evolving network.

Topological constraints. Constraint enforcement provides control over the candidate tree topology after structural optimization. In case the best candidate tree violates a structural constraint (for example, segment intersection), it is removed from the candidate list and the next best solution in the stack is examined. Multiple exclusion constraints can be enforced or combined with AND or OR logic. Topological constraints avoid segment collisions between previously generated branches or to all segments of a complimentary venous tree. Useful implementations include “segments too long”, “too short”, “angle too blunt”, “too acute”, etc …

Microcirculatory closure strategy. The crucial innovation of the proposed microvascular closure rests on two advantageous implementation ideas: (i) deployment of *TerminalNodeSampleGenerator* that guarantees closure segments find all open terminals in arterial and venous trees and (ii) maintenance of binary tree logic of arterial and venous networks during closure. The *TerminalNodeSampleGenerator* uses an emptying index list to avoid repetitious connections to the same terminal. We usually prefer to connect one segment of the arterial tree followed by one segment in venous tree, so that tree growth and diameter updates are spatially balanced. If desired, arterial and venous trees can be fused into a single network for graphical display or further computational purposes.

For a realistic microcirculatory network, it is necessary to adjust tortuosity, which can be achieved by a Bezier Spline approach introduced in previous work [27]. More details on microcirculation can be found in part II of this series.

3. Applications and results

3.1. Simple application of open arterial trees

Fig. 3 demonstrates the versatility of confining vascular growth to arbitrary shapes. For example, Fig. 3A shows the letters LPPD - the acronym of our lab - serving as a highly irregular template to grow balanced arterial trees covering the letter-shaped domain. Note that synthetic arterial trees entwining each letter are perfectly balanced, so that all terminals discharge equal amounts of blood. The circular triangular surface mesh sample generator in Fig. 3B confines growth to a flat disc. Fig. 3C depicts a cubic tissue sample with a partial view of the pial surface arteries, the penetrating arterioles, and a few hierarchies of branching arterioles.

3.2. Synthesis of closed cortical blood supply with microcirculatory closure

Most prior work produced arterial trees without physiological connection to the microcirculation or the venous drainage. This case study illustrates the synthesis of the complete circulation of the somatosensory cortex in mouse. It proceeds through five stages with outcomes presented in Fig. 4 and pseudocode given in supplement B. In step-1, the leptomeningeal arteries and veins are synthesized with methods described in Section 2.2. To ensure anatomically consistent surface coverage by leptomeningeal blood vessels, we control the number of penetrating arteries [4] in the strategy (here 12–14

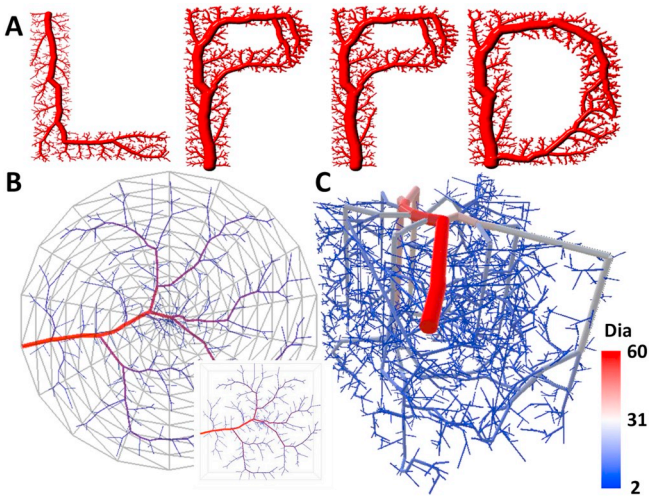

Fig. 3. Synthesis of open arterial structures with sample generators. (A) To show the versatility of the algorithm, the letters LPPD-the acronym of our lab – served as a highly irregular template to grow balanced arterial trees covering the letter-shaped domain. Note that each terminal node discharges exactly the same amount of fluid. (B) A flat arterial tree was created on a disk using a two-dimensional triangular mesh. (C) A snapshot of an incomplete subcortical arterial network grown with the help of a 3D unstructured *CarthesianMeshSampleGenerator.*

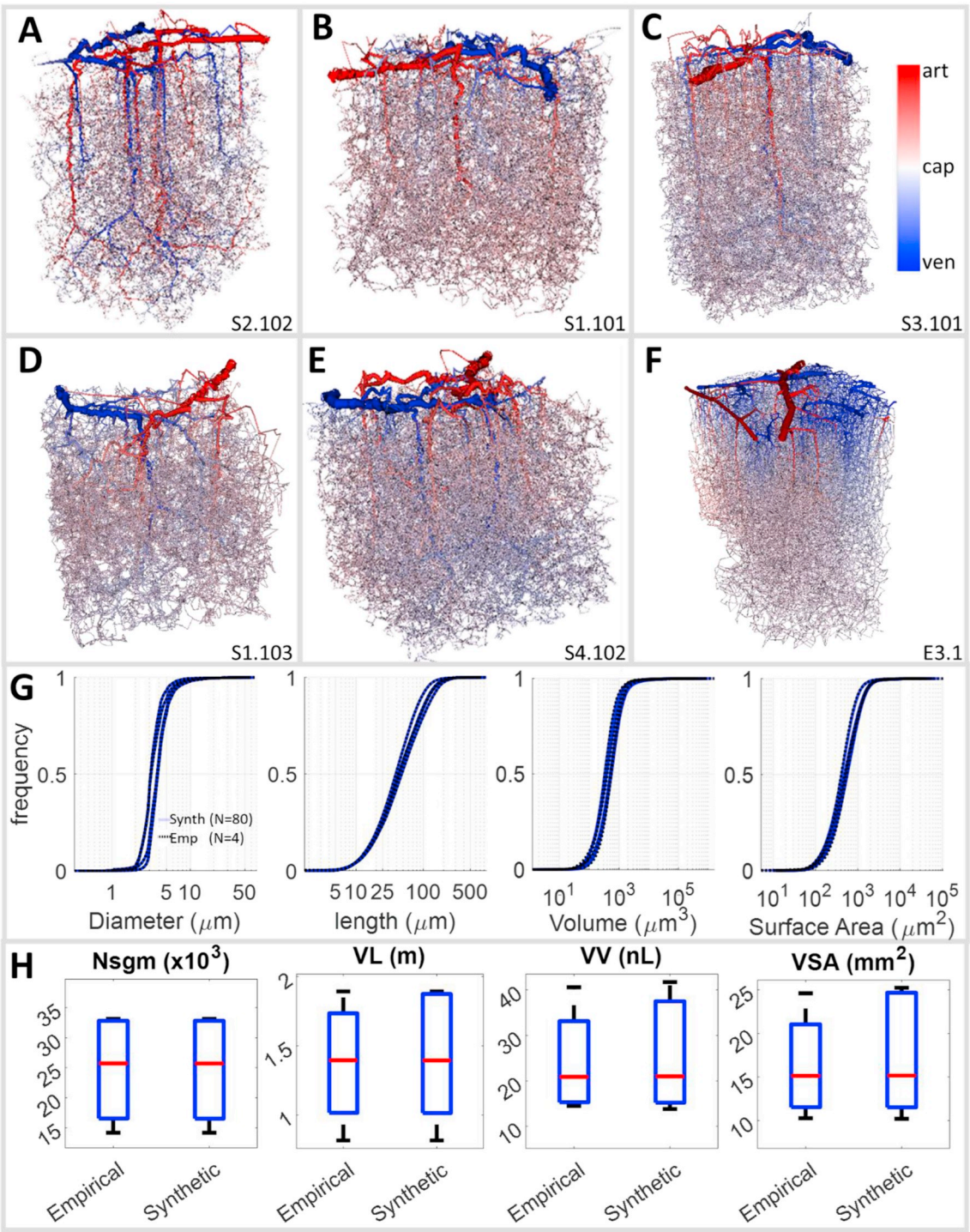

Fig. 4. A collection of synthetic microcirculatory networks of the somatosensory cortex in mouse. (A)-(E) show synthetic structures (S2.102, S1.101, S3.101, S1.103 and S4.102) that were generated to match 2PLSM samples with similar morphometric statistics [4]. Note, red indicates arteries, blue corresponds to veins and white shows capillaries. (G) The statistical properties (CDFs of diameter, length, volume and surface area) of experimental (N = 4, dotted black line) and synthetic (N = 80, transparent blue line) datasets are reasonably aligned. For comparison, frame (F) shows an original 2PLSM dataset (E3.1), which looks similar to the synthetic ones. (H) The cumulative statistics for the empirical and synthetic networks are comparable (comparison between number of total segment count, Nsgm, accumulated vascular length, VL, total vascular volume, VV, and total endothelial surface area, VSA).

penetrating arteries per mm^2). The number of veins was set between 13 and 39 veins per mm^2 in accordance to morphometric data acquired from the 2PLSM data, which also agrees with prior literature values [4,39]. The cortical synthesis is informed by a database of values obtained from the open literature with key entries listed in Table 2. Step-2 ensures that the territories of the main leptomeningeal trunks are oriented perpendicular to the cortical surface. We use *LineNumberGenerator* that create endpoints vertical to the cortical surface up to a depth of 1 mm. The *addSegment* procedure attaches a straight vertical segment at a specific arterial pial terminal. In step-3, subcortical arterial segments grow off main penetrating vessels by volume minimization until a segment count of about half of the total segment

Table 2
Physiological parameters necessary for anatomical growth in mouse.

Parameter	Value	Units	Source
Penetrating arterioles (PA) count	12–13	Nsgm/mm^2	[4]
Ascending venule (AV) count	13–39	Nsgm/mm^2	[4]
PA/AV ratio	1.0–3.0	–	[4]
MCA root diameter	143 ± 8	μm	[40]
ACA root diameter	138 ± 9	μm	[40]
PCA root diameter	121 ± 6	μm	[40]
Brain volume	453 ± 19	mm^3	[41]
	509 ± 23	mm^3	[42]
	415 ± 24	mm^3	[43]
Sagittal length	10–14	mm	[43–46]
Axial height	8–10	mm	[43–45]
Coronal width	5–6	mm	[43–46]
Cortical surface area	380 ± 20	mm^2	[41]
	348 ± 3	mm^2	[42]
Splined segment count (Nsgm)	11,474 ± 1,216	Nsgm/mm^3	[4]
Cortical thickness	1139	μm	[4]
	1154 ± 7	μm	[47]
	1210	μm	[48]

number is reached. Note, the penetrating arterioles and ascending venules branch in a tree-like fashion into the capillary bed. In step-4, the incomplete, not yet confluent arterial and venous sides of the network are sequentially connected by the microvascular closure. From each terminal arterial node, exactly one segment is grown to a close microsegment of the venous side. In analogue fashion, venous terminals are grown to near arterial capillary segments, step-5. Thus, microcirculatory closure adds Nterminals*2 additional microvascular segments.

Tortuosity. Many microvascular segments do not conform to straight cylindrical shapes but exhibit significant tortuosity. We imposed a tortuosity of τ=1.1–1.81 for segments in the d < 150 μm diameter range to create realistic microvessels. Anatomical consistency was imposed by matching the cumulative density functions of the synthetic and corresponding empirical network. Tortuosity was added to the synthetic networks within each bin until the two CDFs agreed.

Validation. Visual inspection of Fig. 4 shows a striking structural similarity between synthetic networks and microcirculatory images (2PLSM) at all hierarchical levels for length, orientation and diameters of pial arteries, to number and direction of penetrating arteries and the connectivity of the tortuous capillary network. Also, the venous subnetworks seem almost indistinguishable.

We also performed detailed statistical analysis of critical morphometic properties in the 2PLSM and synthetic networks. Fig. 4 shows very close statistical agreement between 80 synthetic networks and four 2PLSM data as measured by the cumulative density functions (CDF) of diameter, length, volume and surface area. In fact, the variation between the four experimental datasets is larger than the difference between synthetic and matching experimental datasets. Moreover, the total count of segments (Nsgm) belonging to pial surface arteries, arterioles, capillaries, venules, and veins are virtually the same. Fig. 4H summarizes additional similarity metrics characterizing critical properties of the entire network (=cumulative structural properties). Specifically, the total vascular length, cumulative vascular volume, and total endothelial surface area show excellent agreement between the synthetic and empirical networks.

Taken together, network connectivity (=assessed by visual inspection) as well as statistical comparison at the segment level (=CDF for segment-to-segment comparison) and total network level (=cumulative properties overall sample comparison) indicate that iCNS is capable of synthesizing artificial microcirculatory networks that match morphometrics of microimaging counterparts. The statistical analysis suggests that the 80 synthetic datasets are statistically equivalent to the four 2PLSM counterparts (=digital twins).

3.3. Mathematical network model of the entire MCA territory

Arterial circulation. Cortical surface growth was achieved by a *SurfaceMeshSampler* customized to delineate the mouse cortex (STL surface mesh generated from a mouse atlas). First, the M1 segment of the middle cerebral artery and the main orientation of the main branches were established using *growth from backbone* as depicted during four stages in Fig. 5. Initially, new arteries were restricted to a close neighborhood of existing arterial branches. This strategy avoided pial arteries cutting into the curved cortical surface, which is not physiological. Optionally, surface adherence of the leptomeningeal segments can be improved by normal projection of the bifurcation points (Bif) to the cortical surface. We precisely controlled the number of pial terminals [4] that connect to penetrating arteries by generating 12–14 terminals per mm^2 on the triangular elements of the cortical *SurfaceMeshSampler*.

For the venous circulation of the MCA territory, we departed from the superior sagittal sinus backbone and traversed in reverse direction of the blood flow towards cortical bridging veins. The backbone also contained anatomical information of the Transverse sinuses (Trs), Caudal rhinal vein (Crhv), and Rhostral rhinal vein (Rrhv), see Fig. 6A. During segment addition, collision avoidance was enforced with *Topological constraint functors.*

The cortical microvasculature was synthesized as described in Section 4.2, but with microcirculatory branch terminal positions drawn by a *VolumeSampler* which penetrated 1 mm into the subcortical tissue. The final network encompasses the complete arterial and venous left middle cerebral artery (LMCA) territory with microcirculatory closure. It covers an area 40 times larger than the pial surface of the 2PLSM data sets. This network spanning the entire MCA territory of the first sample, SMCA1.101, totaled 11,092 arteries, 11,206 veins, and 433,042

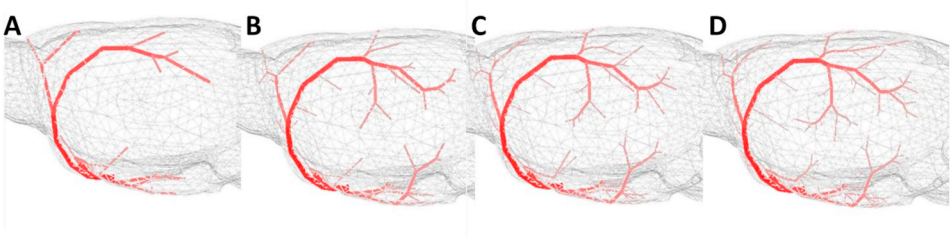

Fig. 5. Four stages of the pial leptomenengial arterial network growth in mouse. The arterial growth was guided by a triangular mesh surface sample generator that delineated the cortical surface, which was reconstructed from in vivo microCT images [28,35]. The SurfaceMeshSampleGenerator uses integer random numbers to generate terminal node samples at the center of STL surface mesh triangles. The smallest pial arteries feeding into penetrating arteries are evenly distributed and discharge the same amount of flow.

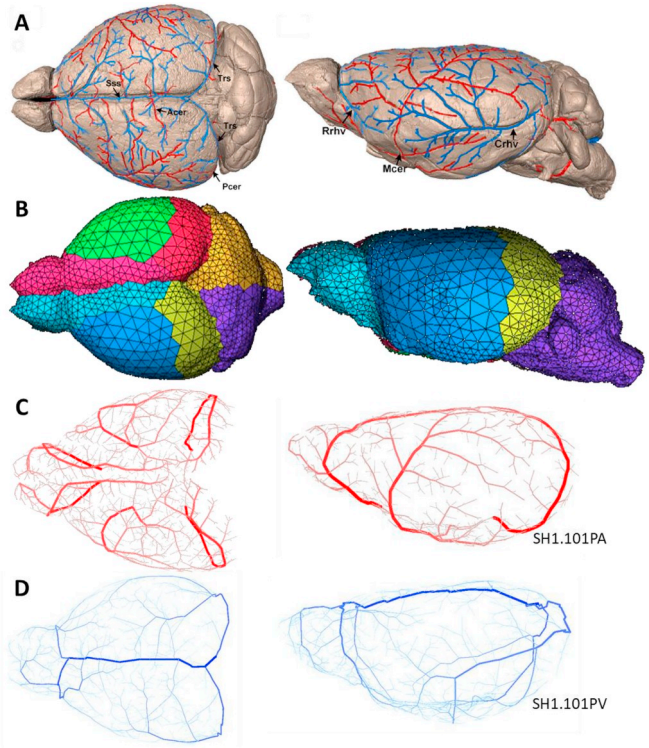

Fig. 6. Comparison of growths with vascular atlas. (A) Arteries (red) and veins (blue) from the Xiong mouse atlas [36]. (B) Cortical surfaces supplied by main cerebral arteries. The colors correspond to different arterial territories; RMCA (green), RACA (pink), RPCA (red), LACA (light blue), LMCA (dark blue), and LPCA (yellow). (C) Synthetic arterial networks and (D) venous circulation for the entire mouse brain (abbreviations: Transverse sinuses, Trs, Caudal rhinal vein, Crhv, and Rhostral rhinal vein, Rrhv). The denomination of SH1.102 signifies the synthetic hemisphere version 102 grown from mouse 1.

capillaries (11,537 segments per mm^3). The statistics of a second MCA territory, SMCA2.101, is given in Table 3. Segment numbers and dimensions agree with our 2PLSM data as well as prior literature data listed in Table 2. The synthesis took less than 2 CPU hours and 6 GB of RAM on a personal computer.

3.4. Cortical blood supply (whole brain circulation)

Fig. 6A displays the intricate circulatory connections from a detailed mouse atlas [36], which we aimed to recreate with a concise mathematical network model. Arterial trees. For the arterial side, orientation and anatomical connectivity of the first few segments of the anterior (LACA), posterior (LPCA) and middle (LMCA) cerebral arteries were supplied as arterial *backbones*, see Fig. 7A. The surface mesh generators were encoded by an STL surface mesh shown in Fig. 6B. The synthetic pial arterial networks are depicted in Fig. 6C. More detailed views of the expanded LACA, LMCA, LPCA territories and venous confluence are depicted in Fig. 7B. The pial networks were constructed with the methods of Section 2.2, but with *SurfaceSampleGenerators* guiding growth along the tilted surfaces of the ACA, MCA and PCA territories. Venous trees. Venous system synthesis for the whole brain required a few adaptations. The venous trees were grown in reverse flow direction. The completed venous networks are depicted in Fig. 6D. Several backbones of the venous circulation depicted in Fig. 7C were assembled from segmented image data. Microcirculation. The microcirculation was created as discussed in Section 2.3. At the smallest length scale, the thinnest microvessels and closure segments are relatively short. For the microscale, it is possible to accelerate performance by replacing the volume optimization objective with a simple nearest segment objective.

Algorithmic complexity of the methodology. For two mice specimen, the cerebral circulation for the left hemispheres with complete cortical circulation were synthesized. The synthetic growth of the complete cerebral circulation for two mouse specimen required approximately 8 CPU hrs on a personal computer and less than 8 GB of memory. Anatomical data for the automatic construction and statistical information for the massive computer model are provided in Table 3.

4. Discussion

We offered a derivation of network synthesis which placed the construction algorithm into a framework of mathematical programming. We introduced a novel methodology to recreate the cortical circulation in the entire mouse brain on a computer. Because anatomical data have limited spatial coverage or resolution, they are insufficient for synthesizing complete mathematical models of functional circulatory networks. This shortcoming was overcome by combining anatomical data with synthetic construction principles. The proposed methodology fills the gaps between data from different length scales pertaining to diverse imaging modalities. Network synthesis can also be used to complement in vivo data sets in the smallest diameter range where imaging data may be unreliable or simply missing. In addition, one can envision applications in which the center of the simulation domain is populated with actual image data but are linked with synthetic microcirculatory models at the boundaries to avoid boundary effects.

We also introduced a novel microvascular closure to connect arterial and venous trees with a realistic capillary bed. A novel *microcirculatory closure* was seamlessly integrated with tree generation principles. We point out that microcirculatory closure can further be accelerated by replacing the volume minimization objective with the nearest neighbor heuristic.

While this paper focuses on image-based circulatory network synthesis (iCNS), its main purpose is not limited to faithful reproduction of anatomical structures, but aims at supporting mathematical modeling of hemodynamic and metabolic functions in the brain. The synthetic anatomical networks are ideal for performing blood flow simulations with some computational results shown in Fig. 8. Biphasic simulations of the cerebral blood flow in the left hemisphere took less than 30 CPU min using preconditioned GMRES and required 13.5 GB of memory. A description of the mathematical modeling of biphasic blood flow and oxygen exchange is beyond the scope of this paper, but is discussed elsewhere [1,28,49–51]. It is important to note that construction principles enforce simplified hemodynamic constraints as a side condition, which leads to remarkably realistic vascular network structures. It is possible to use more complex viscosity laws for synthesis. For example, Coutey et al. [52] used constrained constructive optimization with diameter-dependent viscosity. Simplified hemodynamic principles used during synthesis phase do not preclude choices for rigorous blood flow simulations after the vascular networks have been generated.

All synthesis algorithms were implemented on inexpensive computer hardware in serial execution. The run time could be drastically reduced by parallel processing. Parallelization is most beneficial in at least two locations: (i) delegate one candidate tree optimization (= volume minimization) of N-closest segment connections to N processors, (ii) run the list of topological constraints, especially collision tests, in separate threads.

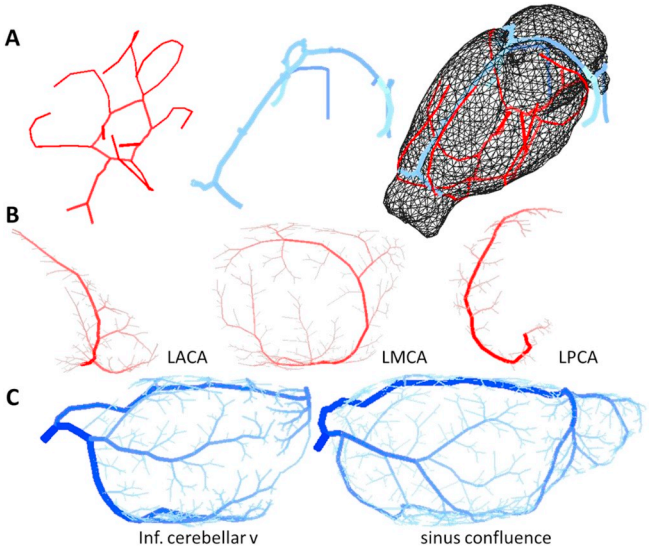

Fig. 7. Illustration of the pial vascular growth for the mouse hemisphere. (A) Cortical surface and initial arterial/venous backbones. (B) Partially completed pial networks grown from backbones for the LACA, LMCA, and LPCA regions. (C) Synthetically grown territory of the inferior cerebellar vein (partial veinous network draining the MCA arteries), and the sinus confluence including the superior sagittal and traverse sinuses. For the arteries of the complete brain, six different backbones are used and later connected to the Circle of Willis.

5. Limitations

In the case studies, morphometric parameters of the growth algorithm of the entire cortical surface were set equal to somatosensory cortex statistics, for which accurate 2PLSM data were available. Several other groups have also produced microanatomical data, but these datasets are not publically available [1,51]. Regional differences in brain anatomy are expected, but these can readily be incorporated by adjusting vessel density and topological constraints, thus not limiting the proposed methodology.

We also noticed the occurrence of very small diameters close to the imaging threshold of the four 2PLSM data sets [4] (some segments have $d < 3\,\mu m$); other authors working with the same data scale the original diameter information to avoid very small diameter occurrence [2]. Since this is a limitation of the diameter reconstruction in the original 2PLSM acquisition and not of the synthesis method, we chose not to alter the original diameters.

For the growth algorithm, we chose constant perfusion pressure and equal terminal node pressure, which caused uniform perfusion of the tissue. Previous studies experimented with variable terminal pressures or flows using probabilistic arguments [21], but the relationship between these more elaborate choices and the impact they had on the structure was not obvious.

6. Conclusions

High resolution image data and construction principles were incorporated in an algorithmic framework for synthesizing anatomically detailed models of the cortical blood supply in the mouse brain. The approach combined the advantages of image segmentation with synthetic network generation. The proposed principles are adaptable for circulatory network generation in other organs. The flexibility for incorporating image data, controlling topological growth with sample generators and the ability to synthesize microcirculatory closures should make the proposed iCNS methodology suitable for other complex anatomical spaces that occur in eye, lung, heart, or kidney.

Mathematical models of cerebral circulation that incorporate anatomically sound morphometric properties are expected to help address open questions regarding blood flow control after neuronal firing (=functional hyperemia), resilience exhibited after stroke (=vascular reserve and collateral blood supply) and autoregulation. The brain-wide scope of the synthetic cortical circulatory networks with anatomically consistent representation of blood vessels spanning multiple length scales is an essential milestone towards computer models able to render mechanistic insights concerning the brain's remarkable adaptability. Based on the encouraging results for the mouse brain, the final goal of creating predictive mathematical models of the *human brain* seems within the grasp of approaches presented in this paper.

Funding

This work was supported by the National Institutes of Health [grant number NINDS 1R21NS099896] and National Science Foundation [grant number CBET-1301198].

Table 3
Statistics for four large synthetic anatomical network structures, specifically two mouse MCA territories (SMCA1.101, SMCA2.101) and two complete hemispheres (SH1.101, SH2.101).

Parameter	MCAs		Hemispheres			
	SMCA1.101	SMCA2.101	SH1.101	SH2.101	Units	Ref
Penetrating arterioles count	13.00	13.03	13.01	13.03	Nsgm/mm^2	[4]
MCA root diameter	142.5	142.5	142.5	142.5	μm	[40]
ACA root diameter	–	–	138.3	138.3	μm	[40]
PCA root diameter	–	–	120.5	120.5	μm	[40]
SSS root diameter	142.5	142.5	250	250	μm	–
Mouse brain volume	238.2	297.9	238.2	297.9	mm^3	–
Sagittal length	13.7	13.7	13.7	13.7	mm	[43–46]
Axial height	8.0	7.9	8.0	7.9	mm	[43–45]
Coronal width	5.5	5.5	5.5	5.5	mm	[43–46]
Cortical surface area	236.8	281.7	236.8	281.7	mm^2	–
Cortical depth	1000	1000	1000	1000	μm	–
Splined segment count (Nsgm)	11,537	11,545	11,518	11,541	Nsgm/mm^3	[4]

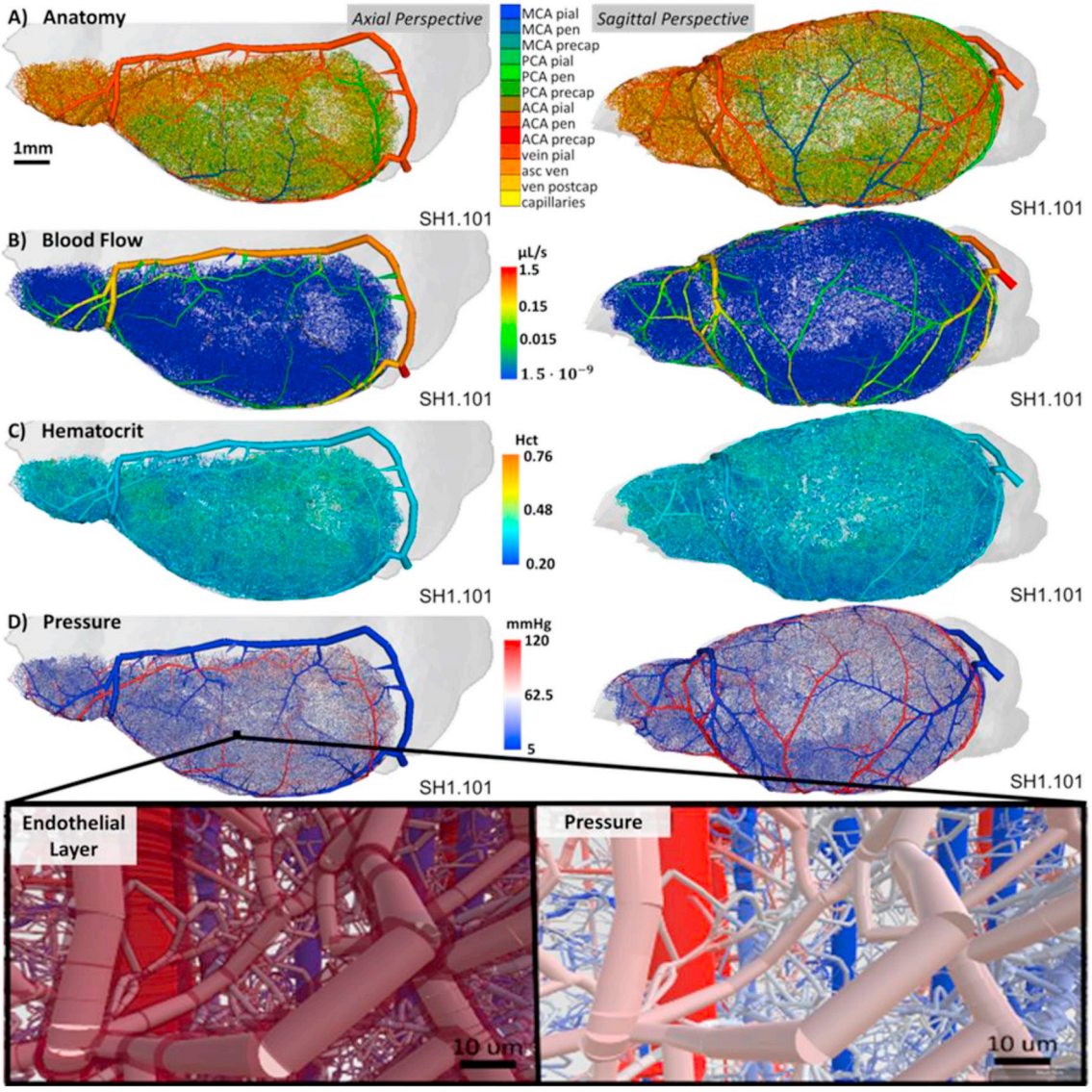

Fig. 8. Network structure and select simulation results from biphasic blood flow for the complete cerebral hemisphere in mouse. (A) The anatomical hierarchy of the network encompasses blood vessels including pial arteries, penetrating arterioles, precapillaries, capillaries, post-capillaries, ascending venules and final drainage through the pial veins and sinuses. (abbreviateions: MCA pial/pen/precap indicates pial vessels, penetrating arterioles and precapillaries belonging to the MCA territory, respectively. Likewise for ACA and PCA. Ven postcap, asc ven, and ven pial indicate venous post-capillaries, ascending venules and pial veins respectively). (B) Blood flow was simulated by solving the hemodynamic flow-pressure equations for the entire hemisphere in less than 30 CPU min for biphasic blood flow. (C) Simulating blood as a biphasic suspension shows cortical depth dependent hematrocrit distribution [28]. (D) The pressure distribution across all territories confirms earlier findings that the largest resistance to blood flow occurs in the microcirculation (E) A zoomed view shows tortuous microvasculature (red-blue) with detailed rendering of the endothelial cell layer (vessel wall) and perivascular spaces (pink). (Note, the segments are rendered as open cylinders because closed parametric surface meshing is computationally very expensive).

Appendix A. Supplementary data

Supplementary data to this article can be found online at https://doi.org/10.1016/j.compbiomed.2019.05.004.

References

[1] Q. Fang, S. Sakadžić, L. Ruvinskaya, A. Devor, A.M. Dale, D.A. Boas, Oxygen advection and diffusion in a three dimensional vascular anatomical network, Optic Express 16 (22) (2008 Oct 27) 17530–17541.

[2] F. Schmid, P.S. Tsai, D. Kleinfeld, P. Jenny, B. Weber, Depth-dependent flow and pressure characteristics in cortical microvascular networks, PLoS Comput. Biol. 13 (2) (2017 Feb 14) e1005392.

[3] S. Lorthois, F. Cassot, F. Lauwers, Simulation study of brain blood flow regulation by intra-cortical arterioles in an anatomically accurate large human vascular network: Part I: methodology and baseline flow, Neuroimage 54 (2) (2011 Jan 15) 1031–1042.

[4] P. Blinder, P.S. Tsai, J.P. Kaufhold, P.M. Knutsen, H. Suhl, D. Kleinfeld, The cortical angiome: an interconnected vascular network with noncolumnar patterns of blood flow, Nat. Neurosci. 16 (7) (2013 Jul) 889–897.

[5] F. Cassot, F. Lauwers, C. Fouard, S. Prohaska, V. Lauwers-Cances, A novel three-dimensional computer-assisted method for a quantitative study of microvascular networks of the human cerebral cortex, Microcirculation 13 (1) (2006) 1–18.

[6] F. Lauwers, F. Cassot, V. Lauwers-Cances, P. Puwanarajah, H. Duvernoy, Morphometry of the human cerebral cortex microcirculation: general characteristics and space-related profiles, Neuroimage 39 (3) (2008 Feb 1) 936–948.

[7] S. Lorthois, F. Cassot, F. Lauwers, Simulation study of brain blood flow regulation by intra-cortical arterioles in an anatomically accurate large human vascular network. Part II: flow variations induced by global or localized modifications of arteriolar diameters, Neuroimage 54 (4) (2011 Feb 14) 2840–2853.

[8] P.S. Tsai, J.P. Kaufhold, P. Blinder, B. Friedman, P.J. Drew, H.J. Karten, et al., Correlations of neuronal and microvascular densities in murine cortex revealed by direct counting and colocalization of nuclei and vessels, J. Neurosci. 29 (46) (2009

Nov 18) 14553–14570.
[9] K. Kidoguchi, M. Tamaki, T. Mizobe, J. Koyama, T. Kondoh, E. Kohmura, et al., Vivo X-ray angiography in the mouse brain using synchrotron radiation, Stroke 37 (7) (2006 Jul 1) 1856–1861.
[10] E.L. Dyer, W.G. Roncal, J.A. Prasad, H.L. Fernandes, D. Gürsoy, V.D. Andrade, et al., Quantifying mesoscale neuroanatomy using X-ray microtomography, eNeuro. 2017 Sep 1 4 (5) (2017) 0195-17.
[11] T. Bicer, D. Gursoy, R. Kettimuthu, I.T. Foster, B. Ren, V. De Andrede, et al., Real-time data analysis and autonomous steering of synchrotron light source experiments, IEEE 13th International Conference on e-Science (e-Science) [Internet]. Auckland: IEEE; 2017 [cited 2019 Feb 11], 2017, pp. 59–68.
[12] M. Zagzoule, J.-P. Marc-Vergnes, A global mathematical model of the cerebral circulation in man, J. Biomech. 19 (12) (1986 Jan 1) 1015–1022.
[13] J.R. Cebral, M.A. Castro, O. Soto, R. Löhner, N. Alperin, Blood-flow models of the circle of Willis from magnetic resonance data, J. Eng. Math. 47 (3/4) (2003 Dec) 369–386.
[14] P.J. Blanco, M.R. Pivello, S.A. Urquiza, R.A. Feijóo, On the potentialities of 3D–1D coupled models in hemodynamics simulations, J. Biomech. 42 (7) (2009 May 11) 919–930.
[15] P.J. Blanco, S.M. Watanabe, E.A. Dari, M.A.R.F. Passos, R.A. Feijóo, Blood flow distribution in an anatomically detailed arterial network model: criteria and algorithms, Biomechanics Model. Mechanobiol. 13 (6) (2014 Nov 1) 1303–1330.
[16] M. Schneider, S. Hirsch, B. Weber, G. Székely, Physiologically based construction of optimized 3-D arterial tree models, Medical Image Computing and Computer-Assisted Intervention – MICCAI 2011 [Internet], Springer, Berlin, Heidelberg, 2011[cited 2018 Mar 5]. pp. 404–11.
[17] W.K. El-Bouri, S.J. Payne, Multi-scale homogenization of blood flow in 3-dimensional human cerebral microvascular networks, J. Theor. Biol. 380 (2015 Sep 7) 40–47.
[18] M. Peyrounette, Y. Davit, M. Quintard, S. Lorthois, Multiscale modelling of blood flow in cerebral microcirculation: details at capillary scale control accuracy at the level of the cortex, PLoS One 13 (1) (2018 Jan 11) e0189474.
[19] S.-W. Su, M. Catherall, S. Payne, The influence of network structure on the transport of blood in the human cerebral microvasculature, Microcirculation 19 (2) (2012) 175–187.
[20] A.V. Bui, R. Manasseh, K. Liffman, I.D. Šutalo, Development of optimized vascular fractal tree models using level set distance function, Med. Eng. Phys. 32 (7) (2010 Sep 1) 790–794.
[21] R. Karch, F. Neumann, M. Neumann, W. Schreiner, A three-dimensional model for arterial tree representation, generated by constrained constructive optimization, Comput. Biol. Med. 29 (1) (1999 Jan) 19–38.
[22] R. Karch, F. Neumann, M. Neumann, W. Schreiner, Staged growth of optimized arterial model trees, Ann. Biomed. Eng. 28 (5) (2000 May 1) 495–511.
[23] R. Karch, F. Neumann, B.K. Podesser, M. Neumann, P. Szawlowski, W. Schreiner, Fractal properties of perfusion heterogeneity in optimized arterial trees: a model study, J. Gen. Physiol. 122 (3) (2003 Sep 1) 307–322.
[24] W. Schreiner, F. Neumann, R. Karch, M. Neumann, S.M. Roedler, A. End, Shear stress distribution in arterial tree models, generated by constrained constructive optimization, J. Theor. Biol. 198 (1) (1999 May 7) 27–45.
[25] W. Schreiner, F. Neumann, M. Neumann, R. Karch, A. End, S.M. Roedler, Limited bifurcation asymmetry in coronary arterial tree models generated by constrained constructive optimization, J. Gen. Physiol. 109 (2) (1997 Feb 1) 129–140.
[26] W. Schreiner, R. Karch, M. Neumann, F. Neumann, S.M. Roedler, G. Heinze, Heterogeneous perfusion is a consequence of uniform shear stress in optimized arterial tree models, J. Theor. Biol. 3 (220) (2003) 285–301.
[27] A.A. Linninger, I.G. Gould, T. Marinnan, C.-Y. Hsu, M. Chojecki, A. Alaraj, Cerebral microcirculation and oxygen tension in the human secondary cortex, Ann. Biomed. Eng. 41 (11) (2013 Nov 1) 2264–2284.
[28] G. Hartung, C. Vesel, R. Morley, A. Alaraj, J. Sled, D. Kleinfeld, A. Linninger, Simulations of blood as a suspension predicts a depth dependent hematocrit in the circulation throughout the cerebral cortex, PLoS Comput. Biol 14 (11) (2018).
[29] B.D.H. Tellegen, A general network theorem, with applications, Philips Res. Rep. 7 (1952) 259–269.
[30] M. Wartmann, Process Network Optimality, Carnegie Mellon University, 2010.
[31] F. Cassot, F. Lauwers, S. Lorthois, P. Puwanarajah, V. Cances-Lauwers, H. Duvernoy, Branching patterns for arterioles and venules of the human cerebral cortex, Brain Res. 1313 (2010 Feb 8) 62–78.
[32] C.D. Murray, The physiological principle of minimum work: I. The vascular system and the cost of blood volume, Proc. Natl. Acad. Sci. Unit. States Am. 12 (3) (1926 Mar 1) 207–214.
[33] C.-Y. Hsu, B. Schneller, A. Alaraj, M. Flannery, X.J. Zhou, A. Linninger, Automatic recognition of subject-specific cerebrovascular trees, Magn. Reson. Med. 1 (77) (2016 Dec 27) 398–410.
[34] C.-Y. Hsu, M. Ghaffari, A. Alaraj, M. Flannery, X.J. Zhou, A. Linninger, Gap-free segmentation of vascular networks with automatic image processing pipeline, Comput. Biol. Med. 82 (2017 Mar 1) 29–39.
[35] S. Ghanavati, L.X. Yu, J.P. Lerch, J.G. Sled, A perfusion procedure for imaging of the mouse cerebral vasculature by X-ray micro-CT, J. Neurosci. Methods 221 (Supplement C) (2014 Jan 15) 70–77.
[36] B. Xiong, A. Li, Y. Lou, S. Chen, B. Long, J. Peng, et al., Precise Cerebral Vascular Atlas in Stereotaxic Coordinates of Whole Mouse Brain. Front Neuroanat [Internet], (2017 Dec 19), p. 11 [cited 2018 Mar 28].
[37] M. Ghaffari, C.-Y. Hsu, A.A. Linninger, Automatic reconstruction and generation of structured hexahedral mesh for non-planar bifurcations in vascular networks, in: K.V. Gernaey, J.K. Huusom, R. Gani (Eds.), Computer Aided Chemical Engineering [Internet], Elsevier, 2015, pp. 635–640 [cited 2018 Mar 7].
[38] E. Gamma, R. Helm, R. Johnson, J. Vlissides, Design Patterns: Elements of Reusable Object-Oriented Software, Pearson Education, 1994, p. 457.
[39] F. Schmid, M.J.P. Barrett, P. Jenny, B. Weber, Vascular Density and Distribution in Neocortex. NeuroImage [Internet], (2017 Jun 29) [cited 2019 Apr 22].
[40] K. Kidoguchi, M. Tamaki, T. Mizobe, J. Koyama, T. Kondoh, E. Kohmura, et al., Vivo X-ray angiography in the mouse brain using synchrotron radiation, Stroke 37 (7) (2006 Jul 1) 1856–1861.
[41] Y. Ma, P.R. Hof, S.C. Grant, S.J. Blackband, R. Bennett, L. Slatest, et al., A three-dimensional digital atlas database of the adult C57BL/6J mouse brain by magnetic resonance microscopy, Neuroscience 135 (4) (2005 Jan 1) 1203–1215.
[42] A. Badea, A.A. Ali-Sharief, G.A. Johnson, Morphometric analysis of the C57BL/6J mouse brain, Neuroimage 37 (3) (2007 Sep 1) 683–693.
[43] N. Kovačević, J.T. Henderson, E. Chan, N. Lifshitz, J. Bishop, A.C. Evans, et al., A three-dimensional MRI atlas of the mouse brain with estimates of the average and variability, Cerebr. Cortex 15 (5) (2005 May 1) 639–645.
[44] A.K. Diem, M. Tan, N.W. Bressloff, C. Hawkes, A.W.J. Morris, R.O. Weller, et al., A Simulation Model of Periarterial Clearance of Amyloid-β from the Brain. Front Aging Neurosci [Internet], (2016) [cited 2018 Mar 22];8.
[45] O. Natt, T. Watanabe, S. Boretius, J. Radulovic, J. Frahm, T. Michaelis, High-resolution 3D MRI of mouse brain reveals small cerebral structures in vivo, J. Neurosci. Methods 120 (2) (2002 Oct 30) 203–209.
[46] F. Clavaguera, T. Bolmont, R.A. Crowther, D. Abramowski, S. Frank, A. Probst, et al., Transmission and spreading of tauopathy in transgenic mouse brain, Nat. Cell Biol. 11 (7) (2009 Jul) 909–913.
[47] S. Lefort, C. Tomm, J.-C. Floyd Sarria, C.C.H. Petersen, The excitatory neuronal network of the C2 barrel column in mouse primary somatosensory cortex, Neuron 61 (2) (2009 Jan 29) 301–316.
[48] J. DeFelipe, L. Alonso-Nanclares, I. Arellano J, Microstructure of the neocortex: comparative aspects, J. Neurocytol. 31 (3–5) (2002) 299–316.
[49] I.G. Gould, P. Tsai, D. Kleinfeld, A. Linninger, The capillary bed offers the largest hemodynamic resistance to the cortical blood supply, J. Cereb. Blood Flow Metab. 37 (1) (2017 Jan 1) 52–68.
[50] I.G. Gould, A.A. Linninger, Hematocrit distribution and tissue oxygenation in large microcirculatory networks, Microcirculation 22 (1) (2015 Jan 1) 1–18.
[51] L. Gagnon, S. Sakadžić, F. Lesage, J.J. Musacchia, J. Lefebvre, Q. Fang, et al., Quantifying the microvascular origin of BOLD-fMRI from first principles with two-photon microscopy and an oxygen-sensitive nanoprobe, J. Neurosci. 35 (8) (2015 Feb 25) 3663–3675.
[52] C. Coutey, M. Berg, H. Ho, P. Hunter, Computational simulation of blood flow and drug transportation in a large vasculature, in: G.R. Joldes, B. Doyle, A. Wittek, P.M.F. Nielsen, K. Miller (Eds.), Computational Biomechanics for Medicine, Springer International Publishing, 2016, pp. 133–142.